



CHORUS

This is the accepted manuscript made available via CHORUS. The article has been published as:

Peierls potential of screw dislocations in bcc transition metals: Predictions from density functional theory

Christopher R. Weinberger, Garritt J. Tucker, and Stephen M. Foiles

Phys. Rev. B **87**, 054114 — Published 28 February 2013

DOI: [10.1103/PhysRevB.87.054114](https://doi.org/10.1103/PhysRevB.87.054114)

The Peierls Potential of Screw Dislocations in BCC Transition Metals: Predictions from Density Functional Theory

Christopher R. Weinberger,^{1,*} Garritt J. Tucker,¹ and Stephen M. Foiles¹

¹*Sandia National Laboratories, Albuquerque, New Mexico 87185-1411, USA*

(Dated: February 4, 2013)

It is well known that screw dislocation motion dominates the plastic deformation in body-centered-cubic metals at low temperatures. The nature of the non-planar structure of screw dislocations gives rise to high lattice friction which results in strong temperature and strain rate dependence of plastic flow. Thus, the nature of the Peierls potential, which is responsible for the high lattice resistance, is an important physical property of the material. However, current empirical potentials give a complicated picture of the Peierls potential. Here, we investigate the nature of the Peierls potential using Density Functional Theory in the BCC transition metals. The results show that the shape of the Peierls potential is sinusoidal for every material investigated. Furthermore, we show the magnitude of the potential scales strongly with the energy per-unit-length of the screw dislocation in the material.

I. INTRODUCTION

The plastic deformation of body-centered-cubic (BCC) metals is well known to be considerably different than closed-packed metals at low temperatures¹. In BCC metals, at nominally quasi-static loading rates and low temperatures, plasticity is controlled by the motion of screw dislocations. Due to high lattice resistance, screw dislocation motion is thermally activated which manifests in a temperature and rate dependent flow¹⁻³.

The high lattice resistance, and hence thermally activated motion, experienced by screw dislocations in BCC metals is a direct result of the non-planar nature of the dislocation core⁴⁻⁷. In contrast, dislocations in close-packed metals on close-packed planes as well as edge dislocations in BCC metals all have low lattice resistance and high mobility⁷⁻⁹. Thus, extensive work exists in establishing the nature of plastic flow in BCC metals as it relates to the structure of the screw dislocation^{6,10-14}.

Empirical atomistic models have been instrumental in confirming the theory of thermally activated flow in BCC metals as well as establishing the core structure of screw dislocations. Notably, all simulations show that the screw dislocation core is non-planar in nature, confirming early arguments based on crystal symmetry. Furthermore, these simulations have shown that the Peierls stress of screw dislocations is high and that dislocation motion is indeed thermally activated. These models have also confirmed the high mobility of edge dislocations in BCC metals, supporting the notion that plastic flow is controlled by screw dislocation motion.

Despite the success of these models, they have not provided a consistent or clear picture of the exact screw dislocation core structure or Peierls potential of BCC metals. Specifically, these simulations have shown two possible types of equilibrium core structures⁵, the compact core which exhibits the full D3 symmetry of the $\langle 111 \rangle$ zone, and the polarized core which only exhibits C3 symmetry (the three-fold rotation axis) and therefore has two degenerate structures related through the $\langle 110 \rangle$ diad. In addition to the predictions of two different equilibrium core structures, these empirical potentials often predict an additional metastable core position¹⁵, the split core¹⁶, to exist between two equivalent compact core structures. This dislocation core lies on a specific $\{110\}$ plane, only obeys the diad symmetry, and is triply degenerate. The existence of the split core structure means there is an additional metastable state as the screw dislocation moves from one compact core to another, which allows for the nucleation of partial kinks along the dislocation line, results in discontinuities in the activation enthalpy as a function of stress^{10,15-17}, and creates a tendency for $\{112\}$ slip¹⁸.

To better understand plasticity in BCC transition metals, recently density functional theory (DFT) has been used to determine dislocation core structures, Peierls stress, and sometimes Peierls potentials. Ismail-Beigi and Arias¹⁹ used DFT to study the core structure of screw dislocations in Mo and Ta and found the core structures to be compact. Similar results have also been found for W, Fe and V²⁰⁻²² and these results do not appear to depend on the pseudopotential or exchange-correlation function. These findings suggest that the equilibrium core structure for pure BCC transition metals is indeed compact.

However, these results do not rule out the existence of the split core, which is a metastable state between two compact cores. Two notable studies have addressed this question using DFT. Segall et al.²² computed the Peierls potential using the drag method (see below for a discussion of the drag method) in Ta using Kleinman-Bylander pseudopotential and the local density approximation (LDA), and demonstrated a metastable configuration, albeit a small one. However, Ventelon and Williams²³ used a projector-augmented-wave (PAW) pseudopotential and the Perdew-Burke-Ernzerhof (PBE) formulation within the generalized gradient approximation (GGA) and showed that

no metastable core structure exists in the Peierls potential in α -Fe. Similarly, Itakura et al.²⁴ also showed a single hump Peierls potential in α -Fe and further showed that the split core structure is unstable. This raises an important question: Which BCC metals exhibit a metastable split core structure and which ones do not? In this paper, we will attempt to determine the existence of the metastable split core structure in BCC metals using DFT. Furthermore, we will use the DFT results to establish how the Peierls barrier height and shape varies across materials.

II. METHODOLOGY

To compute the energy of the dislocations, we use DFT as implemented in the Vienna Ab-Initio Simulation Package (VASP)²⁵. Most of the pseudopotentials used are of the PAW²⁶ type and the exchange correlation (XC) energy is evaluated using the PBE formulation²⁷ within the GGA. However, for Ta, we also consider the Vanderbilt ultrasoft pseudopotentials (USPP)²⁸ and the LDA. The lattice constants were determined using 2 atom supercells with a 400 eV cutoff and high ($31 \times 31 \times 31$) Monkhorst Pack (MK) integration scheme in k-space. The lattice constant, which is listed in Table I, is fixed for all further calculations, while the cohesive energy and elastic constants were determined for this configuration as well.

The number of valence electrons i.e., those that are treated explicitly in the calculations, varies for different materials. For Mo and W, the 6B elements, we use 6 valence electrons. Thus, for Mo we use a Kr core and a Xe core for W. For Ta, we use 5 valence electrons and hence a Xe core. However, for Nb and V we use 11 electrons; this formulation includes the 6 p electrons from the next lowest electron shell. The reason for using a high electron count for Nb and V is that DFT calculations tend to poorly predict C_{44} for all BCC transition metals, particularly for V and Nb²⁹⁻³¹. This inadequacy, as compared to experimental values³², is also observed for LDA calculations²⁰. We used the 5 valence electrons for V and found that C_{44} was 10.8 GPa, compared to the 22.0 GPa found with 11 electrons and 25 GPa with 13 electrons. The origin of the failure of DFT to correctly represent C_{44} in certain approximations is still undetermined^{30,31}. However, the use of the 11 electron formulation is a good balance between accuracy and computational cost. Furthermore, as we will show later, the Peierls potential scales strongly with the elastic constants so the DFT estimated Peierls potential can be corrected using experimental elastic constants.

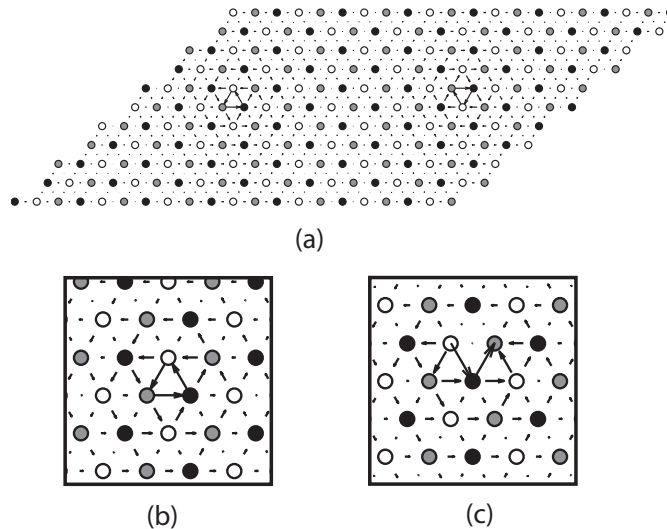


FIG. 1: (a) A differential displacement map of the dislocation dipole used in all of the DFT and EAM simulations. This particular configuration shows the compact core. (b) A close up view of the compact core and (c) the split core structures. Note that the arrow magnitude in (a) and (b) is normalized by $b/3$ while the normalization in (c) is $b/2$.

To determine the properties of screw dislocations in the material modeled, we use a periodic supercell that contains 231 atoms as shown in Figure 1(a) and is described in detail by Li et al.³³. The advantage of this particular supercell is that it actually represents a nearly-square dislocation quadrupole. The dipole configurations are often used because an isolated dislocation is incompatible with periodic boundary conditions. A dislocation dipole was introduced into the simulation cell and the ions were allowed to relax to their equilibrium ground state positions using a 400 eV energy cutoff and a MK integration scheme of $1 \times 1 \times 13$, with high integration along the Burgers vector direction. A differential

displacement map of the screw dislocation dipole is shown in Figures 1(a) and (b) using an empirical potential, however the cores structure is visually indistinguishable from those predicted by all of the DFT simulations of Ta. It is worth noting that this structure, the compact core, was observed in every material tested, which includes Ta, Mo, W, V and Nb. We believe this is the first report of the core structure in Nb using DFT, while our results confirm all previous reports of the compact core in the other BCC materials.

The Peierls potential was computed by determining the transition pathway from one equilibrium dipole structure to another with the dipole uniformly translated along the $\langle 112 \rangle$ direction. This represents motion along a $\{110\}$ plane. The energy pathway was determined using the drag method³⁴ where the reaction coordinate used is the vector from the initial to the final position. The advantage of this reaction coordinate choice is that it is easy to implement and the reaction coordinates correlate with the physical position of the dislocation core, which will become important for determining the shape of the Peierls potential. Furthermore, since the drag method relaxes the forces orthogonal to the drag reaction coordinate, each replica can be run as an individual simulation. Therefore, the drag method is easier to use on large computational clusters as compared to other methods, such as the nudged-elastic-band (NEB) method^{35,36}, that require simultaneous evaluations of each replica. A detailed comparison of the reaction pathways produced by these two methods is discussed below.

III. RESULTS

A. Empirical Potentials

Prior to investigating the results from DFT, it is instructive to use an empirical potential to compare the reaction pathway computed for a dipole configuration to an isolated dislocation, as well as to compare the drag method to the NEB method. To this end, we analyze the energy barrier of screw dislocation motion modeled in Ta using the EAM model parameterized by Zhou et al.³⁷. We consider precisely three cases. First, an isolated screw dislocation is created in a square block of atoms using the displacement field from anisotropic elasticity with the outer atoms fixed, a procedure well outlined in the literature^{6,15,38}. The energy barrier is computed between two equivalent compact core structures using the NEB method, which is shown in Figure 2 (NEB-isolated). The second case (NEB-dipole) is a dislocation dipole with 231 atoms, the same as described in Section II, whose reaction pathway is also determined using the NEB method. Finally, the third case (drag-dipole) is the same dipole as the second case, but the reaction pathway is determined using the drag method.

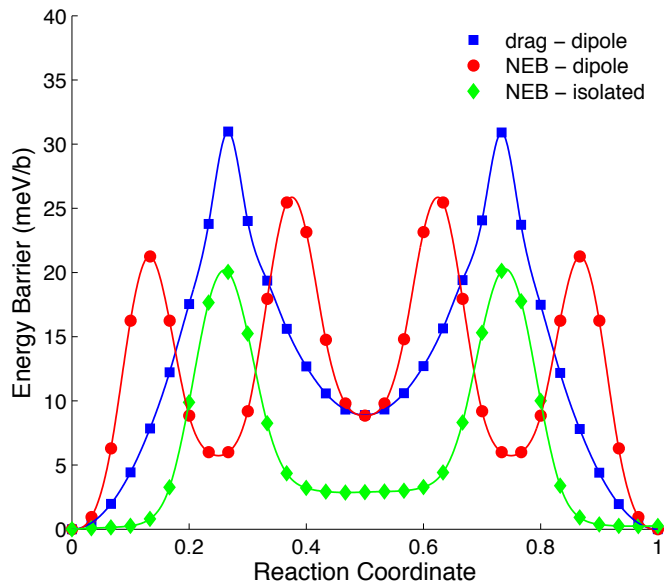


FIG. 2: The energy barrier computed using the EAM potential parameterized by Zhou et al. using both an isolated dislocation and a dislocation dipole. The dislocation dipole configuration energy barrier pathway was computed using both the NEB (NEB-dipole) method as well as the drag method (drag-dipole) while the isolated dislocation reaction pathway was only computed using the NEB method (NEB-isolated).

Figure 2 shows the three different reaction pathways. The isolated dislocation shows a pathway that is common for many EAM potential that predict an equilibrium compact core: there is a clear metastable core configuration midway along the path which corresponds to the split core¹⁶, Figure 1(c). This potential shape has been termed the “camel hump” Peierls potential^{7,39,40}. The two pathways for the dipole configurations also exhibit a metastable core structure midway along the pathway. However, we note that the NEB method applied to the dislocation dipole is able to identify additional metastable states along the path, which are not present in the path predicted by the NEB method for the isolated dislocation or the path predicted by the drag method for the dipole.

This additional metastable state corresponds to the configuration where one of the dislocations is a compact core, Figure 1(b), and the other is a split core structure, Figure 1(c). This can be easily understood as a result of the dipole configuration. The final and initial configurations are screw dislocation dipoles separated by a unit lattice translation along the $\langle 112 \rangle$. Midway along the reaction pathway, the metastable configuration is both dislocations exhibiting the split core structures. The new metastable states, which occur at both the 1/4 and 3/4 reaction coordinates, are comprised of one compact core and one split core. The mixed split core - compact core dipole has a lower separation width, which reduces the elastic energy creating a new metastable state. Thus the motion of the compact core dipole to compact core dipole consists of a simple path: one compact core transitions to a split core, then the other compact core transitions to a second split core, then one of the split cores becomes compact, and finally the last split core becomes compact. This is exactly the reaction pathway observed in the NEB simulations.

The drag method misses the mixed compact-split core structure, which can be inferred from the energy barrier curves in Figure 2. The reason the drag method misses these additional metastable states is because relaxation only occurs normal to the reaction coordinate, which in this cases is a linear interpolation of the dislocation positions. Thus, the drag method will prevent the dislocation cores in the dipole from moving closer together, which is required to capture these new metastable states. However, these additional metastable states can be considered an artifact of the dipole configuration as they do not exist for an isolated dislocation. Since we are interested in predicting the energy pathway as close to the isolated dislocation as possible using the dipole configuration, the drag method has an advantage over the NEB method in this special case. The differences between these two methods as applied to the dislocation dipole are very likely a result of the metastable split core and it remains to be seen if there is a significant difference between the drag and NEB methods if the split core is not stable.

B. DFT Predictions

Prior to studying the Peierls potential across a number of the BCC transition metals, we first take an in-depth look at the Peierls potential specifically in Ta. The effects of the XC function and pseudopotential are investigated in Ta by considering three cases: PAW-PBE, PAW-LDA and USPP-LDA. In each case, the drag method was used to compute the energy barrier. The results of these calculations are shown in Figure 3.

The first observation that can be made is that the Peierls potential shape appears independent of the XC function and the pseudo-potential. The predicted Peierls potential shape is a single hump and appears sinusoidal. While the height of the Peierls potential seems to vary by around 30% with the LDA predicting a larger Peierls potential, the results seem rather consistent between the different parameterizations. However, the Peierls potential shape predicted here appears to contradict the results of Segall et al.²² who found a metastable core along the Peierls potential pathway. It is worth pointing out that those authors used a pseudopotential of Kleinman-Bylander form in conjunction with the LDA approximation of the XC energy, which may predict such a metastable core configuration. While this may suggest a Peierls potential shape dependence on the pseudopotential, the more modern PAW pseudopotentials are expected to be more reliable in predicting the correct electronic structure, suggesting that the results obtained here are likely more reliable.

When the EAM potential was used to describe the Peierls potential in the dipole configuration, we observed very different reaction pathways when comparing the drag and NEB methods. To check the predictions of the Peierls potential on the method of reaction pathway analysis, we use the NEB method once on the dislocation dipole in Ta as described by the PAW-PBE. The results of this calculation are also shown in Figure 3. Here, we see that the two predicted paths (drag and NEB) are very close, with the results of the NEB method showing a height that is only about 15% lower than that predicted by the drag method. Thus, it appears that when a single hump Peierls potential is predicted, the drag method and NEB method both show very similar Peierls potential profiles for the dislocation dipole configuration.

In all of the previous simulations, we have used a cell containing 231 atoms and it is natural to reflect on the potential size effects of using such a small number of atoms in a dipole configuration. For example, it has been shown in dipole configurations that periodic images result into a conditional convergence of the long range elastic fields⁴¹. In our work, the Peierls potential is computed as the difference between two equivalent dislocation dipoles, so this problem is avoided as the long range elastic fields are removed. In addition to long range elastic fields, recent work^{42,43} has

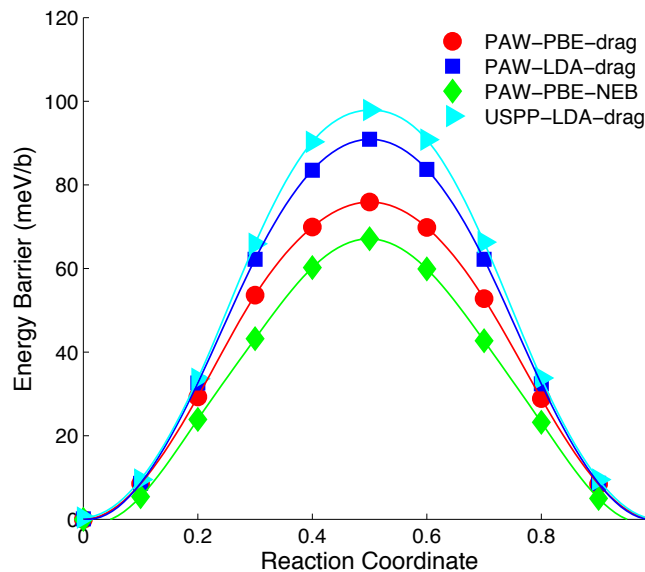


FIG. 3: The Peierls potential computed for Ta using DFT. The four curves represent the comparison of the Peierls potential for different XC functions (PBE and LDA), different pseudopotentials (PAW and USPP) as well as different reaction pathway analysis (drag and NEB). The Peierls potential shape appears universal and the height appears to vary by about 30%, with the largest variation based on the XC function.

shown that the core fields can create errors in the computed dislocation core energies. However, the authors showed that if a quadrupolar dislocation array is used, as is done in this work, the difference in core energies between hard and easy cores exhibit rapid convergence⁴². To verify that this occurs in our simulations and thus demonstrate that size dependent errors are unlikely, we also computed the Peierls potential in Ta using the PAW-PBE for dipoles containing 105 and 405 atoms. The Peierls potential height was computed using the drag method and the values were found to be 92.0 meV/b and 76.1 meV/b. When compared to the 231 atom simulation, which has a Peierls potential of 75.9 meV/b, we find the 105 atom simulation overestimates the Peierls potential by $\sim 20\%$ while the 405 atom simulation is essentially the same. Thus, the 231 atom simulation appears to strike a balance between computational cost and accuracy and is consistently used for the rest of the simulations.

To further investigate the Peierls potential in all of the BCC transition metals, we use the PAW pseudopotential and the PBE formulation of the XC energy with the reaction pathway determined using the drag method. The number of electrons treated explicitly is discussed in the Methodology but includes 6 electrons for Mo and W, 5 for Ta, and 11 for V and Nb. It is worth pointing out that we also used a 5 electron V model, and we will discuss the differences in-depth later.

Figure 4 shows the Peierls potential shape of the 5 different BCC transition metals considered here: Mo, Ta, W, V, Nb. The Peierls potentials are all normalized such that the maximum value is one. For comparison, we have also plotted three different theoretical Peierls potential shapes: a sinusoidal potential, the Eshelby potential⁵⁶ and the anti-parabolic potential⁵⁷; for details see^{2,3}. From these results we can see that all of the BCC transition metals predict a similar Peierls potential shape. At first glance, the shape appears to agree very well with the sinusoidal potential, although the Eshelby potential is also very close. The shape of the Peierls potential computed for all of the Ta methods in Figure 3 also fit the sinusoidal shape as well, suggesting that Peierls potential shape is independent of the reaction pathway analysis. While this result may not appear at first to be very surprising as a sinusoidal potential is an obvious choice, Hirth and Lothe³² have pointed out that this is a model potential and may not accurately describe the potential shape in real materials. Furthermore, the empirical potentials, as noted here and shown in other studies^{15,16}, often predict a double maximum (camel hump) Peierls potential. Thus, the prediction of a common sinusoidal potential may be regarded as quite surprising.

The height of the Peierls potential, which is related to the Peierls stress, appears to vary dramatically from material to material as listed in Table I. Even though this value is for a dislocation dipole, it should be representative of an isolated dislocation²³. One important question to ascertain is how the Peierls potential scales across materials. We investigate this by calculating the correlation coefficient between the Peierls potential height and several quantities associated with the host crystal: the lattice constant, cohesive energy, C_{44} , the cohesive energy divided by the lattice constant and the pre-logarithmic energy factor (computed using anisotropic elasticity theory⁴⁴). The computed

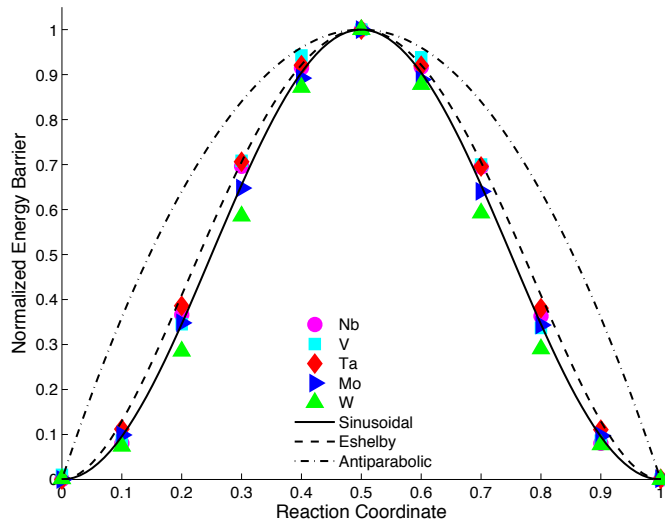


FIG. 4: The Peierls potential for a number of BCC transition metals normalized by the peak value using PAW-PBE as determined using the drag method. Three different theoretical Peierls potential shapes are plotted as well for reference: A sinusoidal potential (solid), the Eshelby potential (dashed) and the anti-parabolic potential (dash-dot).

TABLE I: The lattice constant, cohesive energy, elastic constants, pre-logarithmic energy factor, the height of the Peierls potential, and Peierls stress for 5 BCC metals. Note that the reported Peierls potential height is for a dipole, the value for an isolated dislocation is half this value.

Material	a_o Å	E_{coh} eV	C_{11} GPa	C_{12} GPa	C_{44} GPa	\mathcal{E} eV/b	Peierls Height eV/b	Peierls Stress GPa
W	3.172	8.48	530	204	136	2.30	188	2.4
Mo	3.151	6.36	483	161	93.7	1.75	122	1.6
Ta	3.310	8.20	269	166	70.9	1.24	75.9	0.86
Nb	3.322	6.93	247	136	17.8	0.716	59.25	0.74
V	2.997	5.37	257	144	22.0	0.470	48.7	0.66

correlation coefficients for each of these measures are: -0.03, 0.59, 0.95, 0.69 and 0.96 respectively. The BCC metals have similar lattice constants, around 3 Å, and thus the lattice constant does not correlate with the Peierls potential. Similarly, there is no strong correlation between the cohesive energy and the Peierls potential. There appears a much stronger correlation if one considers the columns of the periodic table independently (5B and 6B) with the Peierls potential increasing with increasing cohesive energy as shown in Figure 5(a). There is also a strong correlation between the elastic constant C_{44} and the Peierls potential without consideration of the column of the periodic table. The one outlier is in the case of Niobium where we can see that the computed C_{44} is lower than that of Vanadium but the Peierls potential is higher.

The Peierls potential height has units of energy per-unit-length, which are not the same as the units of C_{44} , E_{coh} or the lattice constant. Therefore, it seems more reasonable to correlate the height with quantities that share this dimensionality, such as the cohesive energy divided by the lattice constant and the pre-logarithmic energy factor⁴⁴ of a screw dislocation. There is a slight increase in the correlation of the cohesive energy divided by the Burgers vector as compared to the cohesive energy alone. In contrast, the pre-logarithmic energy factor shows a very strong positive correlation with the Peierls potential (as in Figure 5(b)). This result is probably not surprising as it simply states that the Peierls potential height, i.e., the energy of the dislocation in the unstable equilibrium position, scales with the energy of the dislocation in its equilibrium state (a notion originally suggested by Suzuki⁴⁵ from simulations using simple inter-row potentials). However, this is still a profound statement as it suggests how the Peierls potential should scale among materials.

To further solidify this argument, it is worthwhile to compare the predictions of the 5 and 11 electron V formulations. The relevant physical properties for 11 electron vanadium are shown in Table I and the 5 electron properties are: $a_o = 2.979\text{Å}$, $E_{\text{coh}} = 5.37\text{ eV}$, $C_{11} = 275\text{ GPa}$, $C_{12} = 142\text{ GPa}$, $C_{44} = 10.8\text{ GPa}$, $\mathcal{E} = 0.282\text{ eV/b}$, and the Peierls potential height is 29.1 eV/b. The Peierls potential height goes up by a factor of 1.67 from the 5 electron to 11

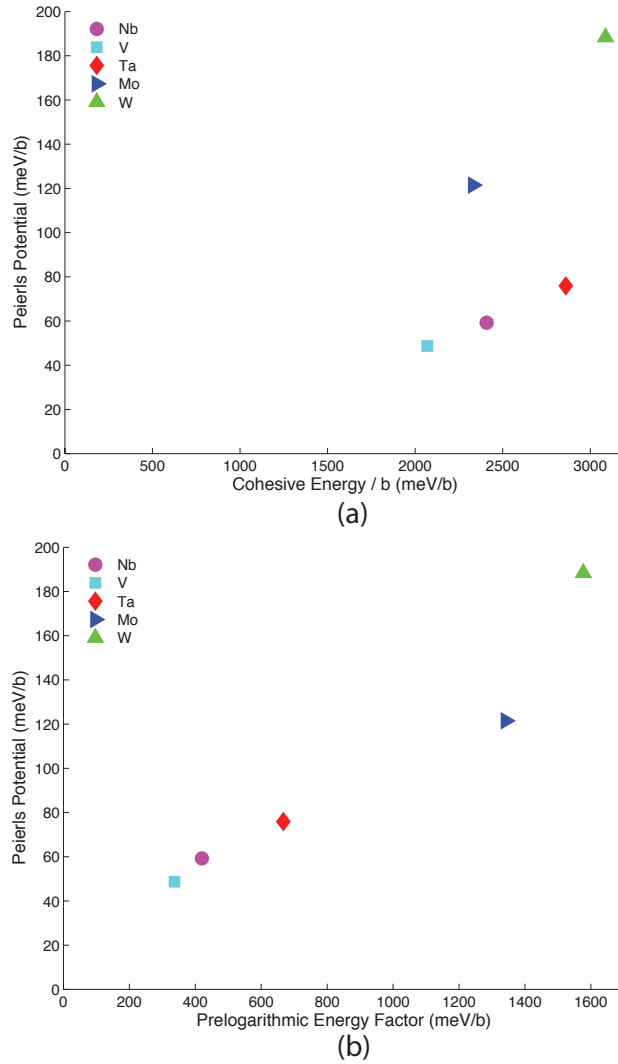


FIG. 5: The computed Peierls potential of the dislocation dipoles plotted against (a) the cohesive energy divided by the Burgers vector and (b) the pre-logarithmic energy factor. The Peierls potential height appears to scale reasonably well with the cohesive energy among elements in the same column of the periodic table and correlates strongly with the pre-logarithmic energy factor of a screw dislocation.

electron formulation while the cohesive energy does not change and C_{44} goes up by a factor of 2.04. This suggests that the Peierls potential height does not scale with the cohesive energy and scales approximately with C_{44} . However, the pre-logarithmic energy factor goes up by a factor of 1.67, the same as the increase in Peierls potential height, providing further support for the idea that the Peierls potential height scales linearly with the pre-logarithmic energy factor.

Given that the Peierls potential has a uniform sinusoidal shape, the Peierls stress, τ_p , can be directly determined from the derivative of the Peierls potential as:

$$\tau_p \equiv \text{Max} \left[\frac{1}{b} \left(\frac{dE}{dx} \right) \right] \quad (1)$$

where E is the Peierls potential and b is the Burgers vector. If we write the Peierls potential as

$$E = \frac{1}{2} \Delta E \left(1 - \cos \left(\frac{2\pi x}{h} \right) \right) \quad (2)$$

where ΔE is the height of the Peierls potential and $h = \sqrt{2/3}a$ is the kink plane height. Here, we note that since the Peierls height computed throughout is for a dislocation dipole, one must use half this height for ΔE when computing

the Peierls stress. The Peierls stress computed for the sinusoidal potential is:

$$\tau_p = \pi \frac{\Delta E}{bh} \quad (3)$$

The values computed from our simulations are listed in Table I and, as expected, scale strongly with the Peierls potential height. These values are a bit lower than those reported in the literature^{21,22} which are obtained by directly straining the lattice. One reason for the lower values is that these Peierls stress calculations are for PAW-PBE and the literature value are for LDA, which typically predicts a higher Peierls potential and hence Peierls stress. However, this cannot explain all of the differences and the main contribution to the low predictions is that the Peierls potential is moderately stress dependent; a feature that is well known from the twinning-anti-twinning asymmetry that arises in the Peierls stress^{6,21}.

IV. COMPARISONS WITH EXPERIMENTS

In the previous section we have shown two important results: the Peierls potential in BCC metals is sinusoidal in shape and the height of the Peierls barrier scales with the dislocation line energy. The first result determines the relationship between the activation enthalpy and the resolved shear stress^{3,46} in the theory of thermally activated flow in BCC metals. This in turn dictates the temperature and strain rate dependent flow stresses at low temperatures^{3,46}. In experiments⁴⁷⁻⁵¹, the flow stress is typically fit using stress-strain rate relationships derived from kink-pair theory assuming that the Peierls potential follows the Eshelby potential; which is very close to the sinusoidal profile that our results support.

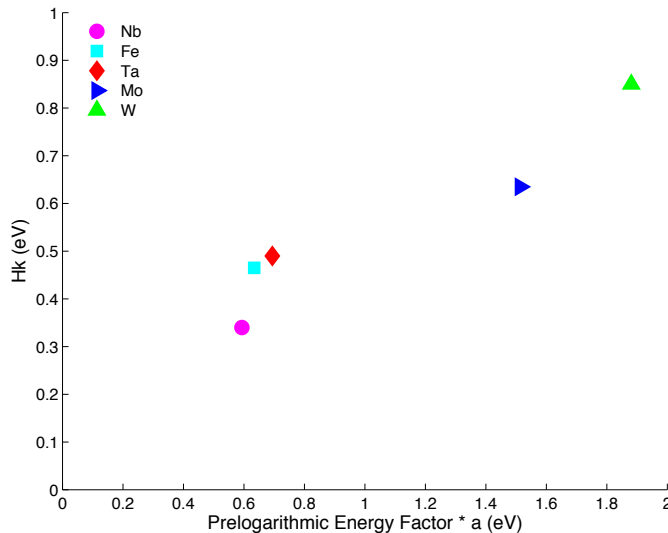


FIG. 6: The experimentally determined kink energy plotted as a function of the product of the pre-logarithmic energy factor times the lattice constant. The approximate linear trends provides experimental evidence that the Peierls potential height scales with the pre-logarithmic energy factor as suggested by DFT calculations.

The second result is that the Peierls potential height scales with the dislocation pre-logarithmic energy factor, which we can further check against experimental measurements of the kink formation energy of an isolated kink. According to elasticity theory, the energy of an isolated kink in a sinusoidal potential can be written as: $U_k = \frac{2^{3/2}}{\pi} h \sqrt{E_o \Delta E}$ where h is the kink height, E_o is the energy per unit length of a screw dislocation and ΔE is the height of the Peierls potential. If we assume $E_o = \mathcal{E} \ln(R/r_o)$ and $\Delta E = C\mathcal{E}$, where C is a constant of proportionality and \mathcal{E} is the prelogarithmic energy factor, we can write a scaling equation for U_k as: $U_k = \frac{2^{3/2}}{\pi} h \mathcal{E} \sqrt{C \ln(R/r_o)}$. Assuming the term inside the square root is not material dependent, we have a scaling relationship between the kink formation energy and the pre-logarithmic energy factor. Since the kink formation energy has been extracted from experiments⁴⁷⁻⁵¹, we can test this scaling relationship directly. To do this we use the kink energies reported in⁵¹ for Ta, Fe, Nb, Mo and W; and we compute the pre-logarithmic energy factors from the elastic constants in³² and multiply them by the lattice constants a_o from⁵². The results of plotting U_k and $a_o \mathcal{E}$ are shown in Figure 6, which exhibits an approximately

linear trend. We note that in the experiments, U_k is determined without assuming a shape of the Peierls potential or elastic constants, it can be determined directly by the strain rate dependence of the critical temperature^{51,53}. The good agreement between the trends observed in experiments with those predicted here illustrates the utility of the DFT simulations conducted herein and validates the proposed general scaling relationship of the Peierls potential.

V. SUMMARY

We used DFT to determine the Peierls potential in 5 BCC transition metals. All 5 metals have a compact screw dislocation core structure, which exhibits the full D3 symmetry of the $\langle 111 \rangle$ zone. The Peierls potential determined in all the simulations was sinusoidal in shape; including both PBE and LDA XC functions, the US and PAW pseudopotentials and considering a variety of the number of valence electrons. No additional metastable screw dislocation core structures were found along the slip transition pathway. This is in agreement with recent DFT calculations of the core structure in iron²³ that showed a Peierls potential that is sinusoidal in shape and lacks a metastable split core structure. These results suggest that empirical potentials are often incorrect, as they frequently predict either a degenerate core structure or a compact core structure along with the split core structure¹⁵. It therefore seems prudent to use the Peierls potential as either part of interatomic potential development in BCC metals or as part of their validation if the potentials are meant to predict properties of BCC screw dislocations, an approach recently taken for the development of BCC iron potentials⁵⁴.

Ultimately, the shape of the Peierls potential is used in the development of kink-pair theory to interpret temperature and strain rate dependent flow stress measurements in BCC metals^{2,46,51}. The work of Seeger^{46,51} has assumed an Eshelby potential for the Peierls potential shape since this form is very close to a sinusoidal potential and admits an analytical relationship between the flow stress, temperature and strain rate. The results presented here suggest that assumed Peierls potential shape, even between different BCC transition metals, is reasonable.

There also appears a clear and strong trend in the height of the Peierls potential as well as the Peierls stress. The Peierls potential height orders such that $W > Mo > Ta > Nb > V$ as predicted by DFT and appears to scale linearly with the energy of a screw dislocation. Despite DFT's inability to precisely predict C_{44} in these materials, the ordering of the Peierls potential heights follows the experimental scaling of the pre-logarithmic energy factor, suggesting this is the order of scaling in the real materials. This simple result suggests that the kink formation energy should also scale with the pre-logarithmic energy factor times the lattice constant. The kink formation energy as determined from experiments does, in fact, scale approximately linearly with this value. This has important implications for determining the effects of simple solid solution alloying. For example, Ta-W alloys are used because they increase the strength and melting temperatures of pure Ta while potentially retaining the ductility of Ta. Thus, using the change of elastic constants based on the solid solution alloy, the Peierls potential height of the alloy can be determined using experimentally determined values of the Peierls heights for the pure elements.

Finally, it is worth pointing out that recent work suggests that mixed $\langle 111 \rangle$ dislocations, i.e. M111 dislocations, also have high lattice friction and may contribute to plastic flow in BCC metals at low temperature⁵⁵. We note that these calculations are performed using the Ackland-Thetford-Finnis-Sinclair potential for Ta that predicts a camel-hump Peierls potential, which may be an artifact of the interatomic model. Thus, this work suggests that mixed $\langle 111 \rangle$ dislocations should be studied by DFT and compared to the results obtained here to better establish their contribution to plastic flow at low temperatures.

Acknowledgments

Sandia National Laboratories is a multi-program laboratory managed and operated by Sandia Corporation, a wholly owned subsidiary of Lockheed Martin Corporation, for the U.S. Department of Energy's National Nuclear Security Administration under contract DE-AC04-94AL85000.

-
- * Electronic address: crweinb@sandia.gov
- ¹ J. W. Christian, *Met. Trans. A* **14A**, 1237 (1983).
 - ² A. Argon, *Strengthening mechanisms in crystal plasticity* (Oxford University Press, 2008).
 - ³ D. Caillard and J. L. Martin, *Thermally activated mechanisms in crystal plasticity* (Pergamon, 2003).
 - ⁴ V. Vitek, R. C. Perrin, and D. K. Bowen, *Philos. Mag.* **21**, 1049 (1970).
 - ⁵ V. Vitek and V. Paidar, *Dislocations in Solids* (Elsevier, 2008), vol. 14, chap. 87, pp. 441–514.
 - ⁶ K. Ito and V. Vitek, *Philos. Mag. A* **81**, 1387 (2001).
 - ⁷ C. R. Weinberger, C. C. Battaile, and B. L. Boyce, *Inter. Mater. Rev.* (2013), in Press.
 - ⁸ M. Duesbery, *Dislocations in Solids* (Elsevier, 1989), vol. 8, chap. 39, pp. 67–173.
 - ⁹ J. Chaussidon, M. Fivel, and D. Rodney, *Acta Mater.* **54**, 3407 (2006).
 - ¹⁰ S. Takeuchi and E. Kuramoto, *J. Phys. Soc. Jap.* **38**, 480 (1975).
 - ¹¹ V. Vitek, *Proc. R. Soc. Lond. A* **352**, 109 (1967).
 - ¹² M. Duesbery and V. Vitek, *Acta Mater.* **46**, 1481 (1998).
 - ¹³ M. Wen and A. H. W. Ngan, *Acta Mater.* **48**, 42554265 (2000).
 - ¹⁴ L. H. Yang, P. Söderland, and J. A. Moriarty, *Philos. Mag. A* **81**, 1355 (2001).
 - ¹⁵ P. A. Gordon, T. Neeraj, Y. Li, and J. Li, *Model. Simul. Mater. Sci. Eng.* **18**, 085008 (2010).
 - ¹⁶ F. Minami, E. Kuramoto, and S. Takeuchi, *Phys. Stat. Sol. (a)* **22**, 81 (1974).
 - ¹⁷ S. Takeuchi, *Phil. Mag. A* **39**, 661 (1979).
 - ¹⁸ L. M. Hale, J. A. Zimmerman, and C. R. Weinberger (2013), submitted.
 - ¹⁹ S. Ismail-Beigi and T. A. Arias, *Phys. Rev. Lett.* **84**, 1499 (2000).
 - ²⁰ S. L. Frederiksen and K. W. Jacobsen, *Philos. Mag.* **83**, 365 (2003).
 - ²¹ C. Woodward and S. I. Rao, *Phys. Rev. Lett.* **88**, 216402 (2002).
 - ²² D. Segall, A. Strachan, W. G. III, S. Ismail-Beigi, and T. Arias, *Phys. Rev. B* **68**, 014104 (2003).
 - ²³ L. Ventelon and F. Willaime, *J. Comput.-Aided Mater. Des.* **14**, 8594 (2007).
 - ²⁴ M. Itakura, H. Kaburaki, and M. Yamaguchi, *Acta Mater.* **60**, 3698 (2012).
 - ²⁵ G. Kresse and J. Furthmüller, *Phys. Rev. B* **54**, 11169 (1996).
 - ²⁶ G. Kresse and D. Joubert, *Phys. Rev. B* pp. 1758–1775 (1999).
 - ²⁷ J. P. Perdew, K. Burke, and M. Ernzerhof, *Phys. Rev. Lett.* **77**, 3865 (1996).
 - ²⁸ D. Vanderbilt, *Phys. Rev. B* pp. 7892–7895 (1990).
 - ²⁹ N. Nagasako, M. Jahnátek, R. Asahi, and J. Hafner, *Phys. Rev. B* p. 094108 (2010).
 - ³⁰ M. F. Salvetti, Ph.D. thesis, MIT (2010).
 - ³¹ L. Koči, Y. Ma, A. R. Oganov, P. Souvatzis, and R. Ahuja, *Phys. Rev. B* **77**, 214101 (2008).
 - ³² J. Hirth and J. Lothe, *Theory of Dislocations* (Krieger, 1982).
 - ³³ J. Li, C. Wang, J. Chang, W. Cai, V. V. Bulatov, K. Ho, and S. Yip, *Phys. Rev. B* **70**, 104113 (2004).
 - ³⁴ G. Henkelman, G. Johannesson, and H. Jónsson, in *Progress on Theoretical Chemistry and Physics*, edited by S. D. Schwartz (Kluwer Academic, 2000), pp. 269–300.
 - ³⁵ G. Henkelman and H. Jónsson, *J. Chem. Phys.* **113**, 9978 (2000).
 - ³⁶ H. Jónsson, G. Mills, and K. W. Jacobsen, in *Classical and Quantum Dynamics in Condensed Phase Simulations*, edited by B. J. Berne, G. Ciccotti, and D. F. Coker (World Scientific, 1998), pp. 385–404.
 - ³⁷ X. Zhou, R. Johnson, and H. Wadley, *Phys. Rev. B* **69**, 144113 (2004).
 - ³⁸ M. S. Duesbery, *Proc. Royal Soc. London A* **392**, 145 (1984).
 - ³⁹ T. Suzuki, H. Koizumi, and H. O. Kirchner, *Acta Metall. Mater.* **43**, 2177 (1995).
 - ⁴⁰ A. Seeger, *Journal de Physique IV* **5**, C7 (1995).
 - ⁴¹ W. Cai, V. V. Bulatov, J. Chang, J. Li, and S. Yip, *Phil. Mag. A* **83**, 539 (2003).
 - ⁴² E. Clouet, L. Ventelon, and F. Willaime, *Phys. Rev. Letters* **102**, 055502 (2009).
 - ⁴³ E. Clouet, L. Ventelon, and F. Willaime, *Phys. Rev. B* **84**, 224107 (2011).
 - ⁴⁴ D.J.Bacon, D.M.Barnett, and R.O.Scattergood, *Prog. Mater. Sci.* **51**, 51 (1978).
 - ⁴⁵ H. Suzuki, in *Dislocation Dynamics*, edited by A. R. Rosenfield, G. T. Hahn, A. L. B. Jr., and R. I. Jaffee (McGraw Hill, 1968).
 - ⁴⁶ A. Seeger, *Z. Metallkd* **72**, 369 (1981).
 - ⁴⁷ L. Hollang, M. Hommel, and A. Seeger, *Phys. Stat. Sol. A* **160**, 329 (1997).
 - ⁴⁸ M. Wernier, *Phys. Stat. Sol. (a)* **104**, 63 (1987).
 - ⁴⁹ D. Brunner and J. Diehl, *Phys. Stat. Sol. (a)* **125**, 203 (1991).
 - ⁵⁰ D. Brunner, *Mater. Trans. JIM* **41**, 152 (2000).
 - ⁵¹ A. Seeger and U. Holzwarth, *Philos. Mag.* **86**, 3861 (2006).
 - ⁵² N. W. Ashcroft and N. D. Mermin, *Solid State Physics* (Brooks Cole, 1976).
 - ⁵³ L. Hollang, D. Brunner, and A. Seeger, *Mater. Sci. Eng. A* **319**, 233 (2001).
 - ⁵⁴ P. Gordon, T. Neeraj, and M. Mendeleev, *Philos. Mag.* **91**, 393 (2011).
 - ⁵⁵ K. Kang, V. V. Bulatov, and W. Cai, *Proc. Nat. Acad. Sci. USA* (2013), in Press.
 - ⁵⁶ The Eshelby potential is: $E = E_o + 16\Delta E \left(\frac{y}{h}\right)^2 \left(1 - \frac{y}{h}\right)^2$.

⁵⁷ The anti-parabolic potential is: $E = E_o + 4\Delta E \left(\frac{y}{h}\right) \left(1 - \frac{y}{h}\right)$.